Blood Pump Design Variations and Their Influence on Hydraulic Performance and Indicators of Hemocompatibility

L. Wiegmann,[1] S. Boës,[2] D. de Zélicourt,[1,3] B. Thamsen,[2] M. Schmid Daners,[2] M. Meboldt,[2] and V. Kurtcuoglu[1,3,4,5]

[1]The Interface Group, Institute of Physiology, University of Zurich, Winterthurerstrasse 190, 8057 Zurich, Switzerland; [2]Product Development Group Zurich, Department of Mechanical and Process Engineering, ETH Zurich, Zurich, Switzerland; [3]National Center of Competence in Research, Kidney.CH, Zurich, Switzerland; [4]Zurich Center for Integrative Human Physiology, University of Zurich, Zurich, Switzerland; and [5]Neuroscience Center Zurich, University of Zurich, Zurich, Switzerland

Associate Editor Ender A. Finol oversaw the review of this article.

Abstract—Patients with ventricular assist devices still suffer from high rates of adverse events. Since many of these complications are linked to the flow field within the pump, optimization of the device geometry is essential. To investigate design aspects that influence the flow field, we developed a centrifugal blood pump using industrial guidelines. We then systematically varied selected design parameters and investigated their effects on hemodynamics and hydraulic performance using computational fluid dynamics. We analysed the flow fields based on Eulerian and Lagrangian features, shear stress histograms and six indicators of hemocompatibility. Within the investigated range of clearance gaps (50–500 μm), number of impeller blades (4–7), and semi-open versus closed shroud design, we found association of potentially damaging shear stress conditions with larger gap size and more blades. The extent of stagnation and recirculation zones was reduced with lower numbers of blades and a semi-open impeller, but it was increased with smaller clearance. The Lagrangian hemolysis index, a metric commonly applied to estimate blood damage, showed a negative correlation with hydraulic efficiency and no correlation with the Eulerian threshold-based metric.

Keywords—Computational fluid dynamics, Ventricular assist device, Centrifugal blood pump, Impeller design, Blood damage, Thrombosis, Hemolysis.

Address correspondence to V. Kurtcuoglu, The Interface Group, Institute of Physiology, University of Zurich, Winterthurerstrasse 190, 8057 Zurich, Switzerland. Electronic mail: vartan. kurtcuoglu@uzh.ch

The authors L. Wiegmann and S. Boës contributed equally to this study.

INTRODUCTION

Ventricular assist devices (VADs) are the main treatment option for patients with end-stage heart failure if heart transplantation is not possible. Even though VADs are increasingly implanted as destination therapy, patients still suffer from high rates of adverse events.[17] Many of these, such as bleeding, thrombosis and stroke, are thought to be closely related to the flow conditions within the VAD. These flow conditions are determined to a large extent by the pump design, which suggests that its optimization would translate to fewer adverse events and improve patients' quality of life.

Among the existing pump types, turbodynamic pumps are most widely used for VADs. Several experimental and numerical frameworks have been devised for their optimization. Studies such as those by Wu et al.[29,30] and Arvand et al.[2] shed light on the impact of different impeller designs and clearance gap sizes, while others have focused on developing automated optimization frameworks.[32,33] Yet, for designers, it is important to gain insight into the impact of single design parameters independently. Building on the vast collective know-how on generic turbodynamic pumps, Mozafari et al. systematically investigated the impact of variations in geometry.[18,22] The latter study[22] focused on hydrodynamic performance, investigating the influence of geometry on a metric for hemolysis.

Computational VAD design studies reporting on hemocompatibility have typically focused on hemolysis[6,11,16,31] represented by a hemolysis index (HI), which incorporates a weighted integration of shear

stresses and exposure times. However, despite being widely used, HI performs poorly in predicting experimentally measured hemolysis values.[27] Its value derives from providing insight into the shear stress history as a general indicator of potential damage to blood cellular components, which may be of use for comparative studies. Thrombus formation as another major aspect of hemocompatibility is driven by multiple factors, including platelet activation and slow blood flow conditions. While an assessment of the latter is indeed feasible, direct computational prediction of platelet activation is currently not possible. Therefore, computationally determinable surrogates have been suggested to serve as alternatives.[9,21] In general, views on the best surrogate metric of hemocompatibility diverge and validated models for predictions of measured values remain a challenge. This may be one reason why metrics applied for assessing blood damage differ between studies on VAD geometry.

In this study, we provide a comprehensive investigation of selected design parameters in view of their hydrodynamic performance and hemodynamic characteristics. Our geometry is based on an industrial pump design guideline,[12] starting from which we investigate the effect of alterations in clearance gap, number of blades, and shroud design. We use computational fluid dynamics simulations that are validated experimentally regarding hydraulic performance to assess the flow fields within the pump, as well as Lagrangian particle tracks to characterize the stress exposure of blood cellular components flowing through the device. These analyses are further supplemented by the classical HI and other metrics proposed to correlate with platelet activation, thrombus formation, or acquired von Willebrand disease. Collectively, these results shed light on the impact of gap size, blade number and shroud design on shear stress exposure and flow stagnation, both of which were shown to have implications in terms of blood damage and thrombosis potential.

MATERIALS AND METHODS

Baseline Pump Design

The impeller and the housing were designed according to the industrial design guideline for centrifugal pumps by Gülich.[12] Starting with six input parameters that describe the desired operating conditions and impeller topology, the design process is broken down into 21 steps, involving 65 equations and look-up tables, which ultimately result in fully constrained geometries of the impeller and housing. De-

tails on this process are given in Supplementary Material A.

The first three input parameters that describe the desired operating conditions were maintained constant for all designs performed in this study: Operating rotational speed and pressure head were set to 3000 rpm and 100 mmHg, respectively. The design flow rate as an input to the design guideline was iteratively increased until, for our baseline geometry, an effective flow rate of 4–5 L/min was achieved in the computational fluid dynamics (CFD) simulation. The chosen speed and pressure head correspond to that of the HVAD (Medtronic/Heartware, Minneapolis, MN, USA), a clinically used VAD that produces a flow rate of 5 L/min against a pressure head of 106 mmHg at 3000 rpm.[5] The simulated effective flow rate in the retained baseline geometry was 4.4 L/min.

The remaining three input parameters for the impeller topology, namely clearance gap size (defined as the distance between the tip of the blades and the housing), number of blades and shroud design, were chosen based on the recommendations given in Gülich.[12] They are listed in Tables 1 and 2 under "Baseline". Figures 1a and 1b show the CAD drawings of the resulting pump, featuring a priming volume of 11 mL and an impeller with 32 mm diameter. Since the character of this study is conceptual, the design process was free of any constraints imposed by bearing and actuation systems.

Design Variations

Starting with the baseline design as the initial configuration, clearance gap size, number of blades, and shroud type were varied independently (Table 1). These variations resulted in a total of eight simulated designs, including the baseline design. Table 2 shows the combination of parameters for each variant. Parameter ranges were chosen based on literature and existing technology. For the size of clearance gap, we selected a lower bound of 50 μm and an upper bound of 500 μm based on the dimension of the smallest gaps between impeller and housing of the HVAD[28] and the HM3 (HeartMate 3, Abbott/Thoratec, Abbott Park, IL, USA),[26] respectively. The number of blades was varied from four as seen in a number of clinically used VADs, including the HVAD and HM3, up to seven in order to investigate the suggested range of five to seven blades based on the specific speed of our pump design.[12] In the third variation, the influence of the presence or absence of a top shroud was examined. A semi-open design has a bottom shroud but no top shroud (like the HVAD), whereas a closed design has

TABLE 1. Investigated geometry parameter values.

Parameter	Value
Clearance gap size	50, 150, **300**, 500 μm
Number of blades	4, **5**, 6, 7
Shroud design	**Semi-open**, closed

The clearance gap size, number of blades and shroud design were investigated independently, varying one parameter at a time while the others were maintained at their baseline value (marked in bold).

both bottom and top shrouds (like the HM3). In both designs, we kept the blade height constant. Therefore, the housing of the closed design was slightly larger to maintain the desired clearance gap, resulting in a 1.6% increase of the priming volume.

Computational Fluid Dynamics Simulations

Computational fluid dynamic simulations were carried out for the eight different designs to evaluate their hydrodynamic performance and associated hemodynamics. The geometries were imported into the commercial CFD package StarCCM+ (Siemens, Munich, Germany). Polyhedral grids were generated using the same settings for all configurations, including a 4-element boundary layer along the walls and a local mesh refinement in the clearance gap, ensuring that it contained a minimum of twelve cell layers. The resultant grid sizes ranged between 4.7 and 7.6 million cells.

The three-dimensional unsteady Reynolds-averaged Navier–Stokes equations were solved using the k-ω-SST turbulence model and implicit second order temporal discretization. Blood was modelled as a Newtonian fluid with a viscosity of 3.5 mPa·s and a density of 1060 kg/m^3. This simplification was considered acceptable, as the non-Newtonian properties of blood, such as shear-thinning, become negligible at high shear rates (> 100 s^{-1})[20] such as those typically found in VADs. The rotation of the impeller was implemented as a rigid body motion with a set speed of 3000 rpm. Pressure boundary conditions were set at the inlet and outlet with a user-defined function such that a constant static pressure head of 100 mmHg was kept between inlet and outlet of the pump.

The simulations were carried out with a convergence criterion of 10^{-4} for the residual errors and a time step of 5 × 10^{-5} s, corresponding to less than 1° rotation per time step at 3000 rpm. The simulations were run

TABLE 2. Combinations of geometry parameters for each simulated design.

Variant	Clearance gap				Number of blades				Shroud design	
	I	II	Baseline	III	IV	Baseline	V	VI	Baseline	VII
Clearance gap size (μm)	50	150	300	500	300	300	300	300	300	300
Number of blades	5	5	5	5	4	5	6	7	5	5
Shroud design	semi-open	semi-open	semi-open	semi-open	semi-open	semi-open	semi-open	semi-open	semi-open	closed

Only one parameter was varied at a time for each of the three parameters: clearance gap, number of blades and shroud design. The baseline design is the same for each of the three variations. This resulted in a total of eight individual designs (including the baseline design) that were evaluated in the CFD simulations.
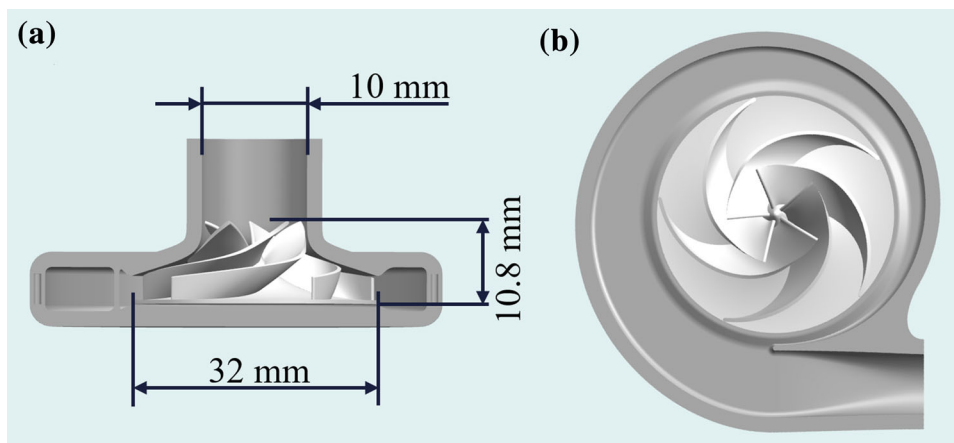

FIGURE 1. (a) Side-view of the CAD model of cut-open housing and impeller design that served as baseline for the CFD simulations, (b) top-view of the CAD model of baseline impeller and cut-open housing.

for five rotations after the flow rate had stabilized, and only the fifth cycle was used for the analysis. Grid and time step independence were confirmed for pressure, velocity, and shear stresses as reported in Supplementary Material B.

To probe blood cell paths through the pump, we implemented a Lagrangian particle tracking with passive advection. The particles had a diameter of 5 μm and a density of 1125 kg/m^3, which are representative of the dimension and density of red blood cells. A total of 6332 particles were seeded 4 mm downstream of the inlet in a uniform spatial distribution during four consecutive time steps.

Validation

To validate the numerical simulations, the hydraulic performance of the baseline pump design was also assessed experimentally. The baseline design was complemented with features for motor shaft integration resulting in only slight geometric changes to the bottom of the housing below the impeller, which was assumed to have no impact on the fluid dynamics. This design was then 3D-printed using photopolymeric resin (FullCure 720, Objet-Stratasys Inc., Eden Prairie, MN, USA) in a polyjet printer (Objet Eden 350 V, Objet-Stratasys Inc.) with a layer thickness of 16 μm. We investigated the surface roughness of the printed material with a confocal laser microscope (VK-X260 K, Keyence International, Mechelen, Belgium) for different inclinations relative to the printing axis, obtaining a mean Ra value of 5 μm. A brushless motor (EC-max 40, 120 W, Maxon Motor AG, Sachseln, Switzerland) was used for actuation. The impeller was mounted directly on the motor shaft through press fit. The 3D-printed pump was connected to the test bench[25] with two pressure-controlled fluid reservoirs, and the resulting flow rate was measured at the pump inlet as illustrated in Fig. 2. The pressure head over the pump was measured with two in-line pressure sensors (TruWave, Edwards Lifesciences, Irvine, CA, USA) connected to the inlet and the outlet of the pump.

Analyses

Table 3 summarizes the metrics used to compare the various design options in terms of hydrodynamic performance and hemodynamic characteristics.

To gain better understanding of the relation between design features and potential blood damage, we investigated the flow fields qualitatively and quantitatively. To this end, we visualized the regions with low velocities, potentially prone for platelet aggregation and thrombus formation,[4] considered disturbances of the flow field, investigated the location of
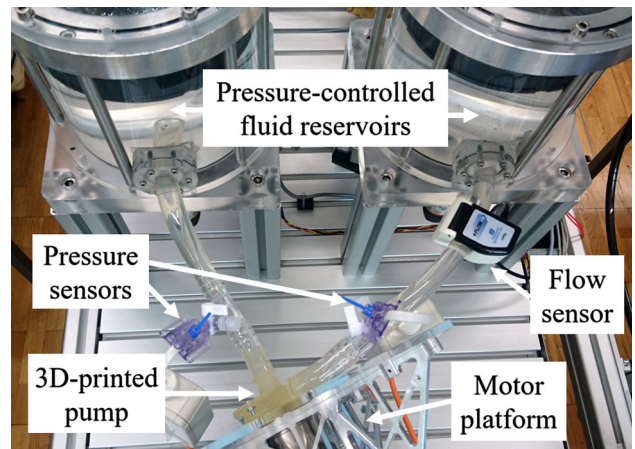

FIGURE 2. 3D-printed baseline pump design on the motor platform, connected to the test bench[25] for experimental validation.

zones with high shear stresses and compared histograms of medium and high shear stresses and exposure times along the Lagrangian particle tracks. We also analysed six metrics proposed in literature to assess blood damage potential that quantify Eulerian and Lagrangian characteristics of the simulated flow fields. Spanwise vorticity and hemolysis index (HI) were integrated over all particle tracks. All other metrics, Eulerian in nature, were computed at each time step and averaged over the last rotation.

Central to most blood damage models are the fluid shear stresses experienced by blood cells and plasma proteins as they flow through the device. The scalar shear stress, τ, was calculated from the viscous shear stress components, σ_{ij}, according to Bludszuweit et al.[3]:

$$\tau = \left[\frac{1}{6}\sum(\sigma_{ii} - \sigma_{jj})^2 + \sum\sigma_{ij}^2\right]^{1/2} \quad (1)$$

Reynolds stresses were not included in the scalar shear stress since blood damage models available in literature are based on viscous stresses only.[27]

HI was calculated as a power law of the scalar shear stresses and exposure time[10] (see corresponding equation in Table 3) using constants by Heuser and Opitz[14] as presented before.[27] Values of HI were integrated along each particle track based on the recorded shear stress histories, and were then averaged to derive the total HI for blood flowing through the VAD. Variation in the number of seeded particles above 6332 (tested range 156–9498) did not result in significant changes in the computed HI.

We further determined the overall volumes of fluid in which fluid shear stress is above the threshold suspected for von Willebrand factor (VWF) cleavage ($\tau > 9$ Pa), platelet activation ($\tau > 50$ Pa) and hemol-

TABLE 3. Summary of the analyzed hydrodynamic and hemocompatibility metrics, their implementation, and their suspected implication for blood pumps.

Metric	Implementation	Implication	Ref.
Pump flow rate (Q_{pump}) [m³/s]	$Q_{pump} = \frac{1}{T_{2\pi}} \int_0^{T_{2\pi}} Q(t)\,dt$	Suitability for full pump support of patient	
Leakage flow rate (Q_{leak}) [m³/s]	$Q_{leak} = \int \bar{v} \cdot \bar{n}\, dA_{gap}$	Efficiency losses	
Hydraulic efficiency (η)	$\eta = \frac{P_{hydr}}{P_{mech}} = \frac{Q_{pump} \cdot H}{T \cdot}$	Hydraulic design	
Relative fluid volume with scalar shear stress above a threshold ($I_{\tau > Thres}$)	$I_{\tau > Thres} = \frac{V_{\tau > Thres}}{V_{total}}$	Hemolysis (Thres = 150 Pa) / Platelet activation (Thres = 50 Pa) / VWF cleavage (Thres = 9 Pa)	9
Relative area of low WSS on the impeller surface ($I_{WSS < 1Pa}$)	$I_{WSS < 1Pa} = \frac{A_{WSS < 1Pa}}{A_{total}}$	Thrombus formation	15
Spanwise vorticity index (SPWVI) [1/s]	$SPWVI = \frac{1}{N_p} \sum_{k=1}^{N_p} \frac{1}{N_k} \sum_{j=1}^{N_k} |SPWV_{k,j}|$ $SPWV(\bar{s};t) = |\bar{w}(\bar{s};t)|\sin(\varphi(\bar{s};t))$	Platelet activation status	21
Hemolysis Index (HI)	$HI = \frac{1}{N_p} \sum_{k=1}^{N_p} C \left(\sum_{j=1}^{N_k} \Delta t_{k,j} \tau_{k,j}^{\beta/\alpha} \right)^{\alpha}$ $\alpha = 0.7650$ $\beta = 1.9910$ $C = 1.8 \times 10^{-6}$	Hemolysis	10,14

$Q(t)$: volume flow rate [m³/s], t: time [s], $T_{2\pi}$: time period for one one rotation [s], $\bar{v}$: fluid velocity vector [m/s], $\bar{n}$: normal of A_{gap}, A_{gap}: surface of gap between impeller and housing [m²], P_{mech}: mechanical power [W], P_{hydr}: hydraulic power [W], Ω: angular speed [rad/s], T: torque on rotor [Nm], H: pressure head [Pa], τ: scalar shear stress obtained from Eq. (1) [Pa], $V_{\tau > Thresh}$: fluid volume with scalar shear stresses above the prescribed threshold [mL], V_{total}: total volume of fluid in the pump [mL], VWF: von Willebrand factor, WSS: wall shear stress [Pa], A_{total}: total surface area of the impeller surface [m²], $A_{WSS > 1Pa}$: area of the impeller surface exposed to WSS above 1 Pa [m²], $SPWV$: local spanwise vorticity [1/s], $\bar{s}$: position vector [m], $\bar{\omega}(\bar{s};t)$: vorticity vector [1/s], $\varphi(\bar{s};t)$: angle formed by velocity and vorticity vector [rad], N_p: number of particle trajectories, N_k: number of points on the k-th particle trajectory, N_k: number of particle trajectories, α, β, C: empirical constants[14].
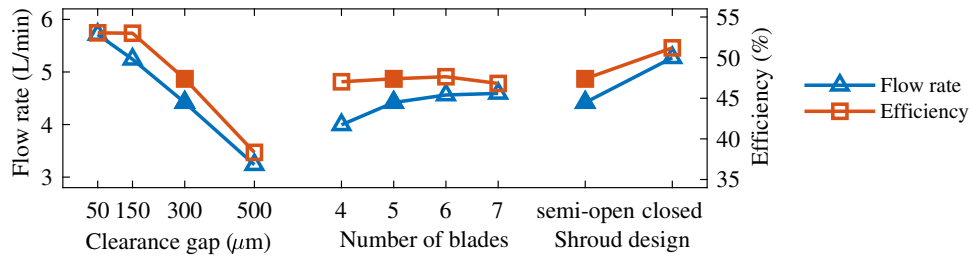
FIGURE 3. Computed flow rate and hydraulic efficiency plotted for variations of clearance gap size, number of blades and shroud design. The baseline configuration is marked by filled symbols. When one parameter was varied, the remaining two parameters were kept at baseline value. Note that the vertical axes depicting flow rate and efficiency have ranges of 3–6 L/min and 35–55%, respectively.
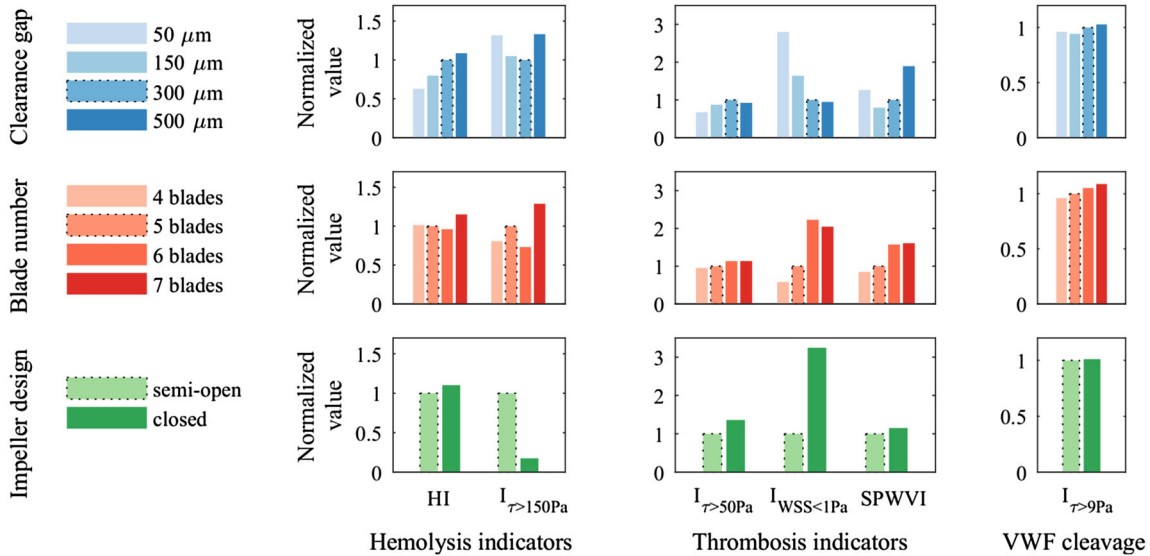

FIGURE 4. Effect of change in clearance gap size (50–500 μm), number of blades (4–7), and shroud design (semi-open or closed) on hemocompatibility indicators. Hemocompatibility indicators are grouped into three categories according to their suspected implications: (1) Hemolysis indicators are HI and $I_{\tau>150Pa}$. (2) Thrombosis potential is indicated by $I_{\tau>50Pa}$, rotor surface with $I_{WSS<1Pa}$ and SPWVI. (3) Bleeding potential due to VWF cleavage is assessed with $I_{\tau>9Pa}$. All indices are normalized by their respective values in the baseline configuration. Numerical values are listed in Supplementary Material C. Dashed frames indicate baseline configuration.

ysis ($\tau > 150$ Pa),[9] respectively. Enhanced VWF cleavage and the successive loss of its high molecular weight multimers is believed to be one of the main causes for bleeding complications in VAD patients.[23] Areas of very low wall shear stress (WSS) on the rotor surface (WSS < 1 Pa) were derived to assess the potential risk of platelet deposition.[15] The Lagrangian spanwise vorticity index (SPWVI) was shown numerically to correlate well with the platelet activation status.[21] This correlation was originally reported for prosthetic heart valves, but since the principles behind shear stress-induced effects on blood components are comparable for blood pumps, an application in this field seems reasonable.[24]

To test for association between blood damage indices suggested in literature, we calculated the non-parametric rank correlation coefficients (Spearman's rho) using the IBM SPSS Statistics 23 software (IBM Corporation, Armonk, USA). *P*-values below 0.05 were considered indicative of statistical significance. We checked visually for the absence of non-monotonic relations.

RESULTS

The influence of design parameter variation on pump flow rate and hydraulic efficiency is shown in Fig. 3. The pump flow rate ranged between 3.2 and 5.7 L/min, and the hydraulic efficiency between 38 and 53%. With 4.4 L/min of flow at 100 mmHg, the baseline geometry achieved an efficiency of 47%. The variation of the clearance gap led to the most sub-

TABLE 4. Spearman's rank correlation coefficients for the hydrodynamic and hemocompatibility metrics obtained by CFD simulations.

		η	Q_{leak}	$I_{\tau>150Pa}$	$I_{\tau>50Pa}$	$I_{\tau>9Pa}$	$I_{WSS<1Pa}$	HI	SPWVI
η	r	1							
	p-value	.							
Q_{leak}	r	−0.48	1						
	p-value	0.233	.						
$I_{\tau>150Pa}$	r	−0.24	−0.36	1					
	p-value	0.570	0.385	.					
$I_{\tau>50Pa}$	r	−0.31	0.50	−0.64	1				
	p-value	0.456	0.207	0.086	.				
$I_{\tau>9Pa}$	r	−0.52	0.26	0.02	0.64	1			
	p-value	0.183	0.531	0.955	0.086	.			
$I_{WSS<1Pa}$	r	0.69	−0.29	−0.14	0.14	0.21	1		
	p-value	0.058	0.493	0.736	0.736	0.610	.		
HI	r	**−0.71***	0.62	−0.12	**0.74***	0.60	−0.24	1	
	p-value	0.047	0.102	0.779	0.037	0.120	0.570	.	
SPWVI	r	−0.50	0.21	0.43	0.21	**0.86****	0.19	0.41	1
	p-value	0.207	0.610	0.289	0.610	0.007	0.651	0.320	.

Statistically significant correlations are highlighted with bold case.

r: rank correlation coefficient, η: hydraulic efficiency, Q_{leak}: leakage flow rate, τ: scalar shear stress, $I_{\tau>150Pa}$, $I_{\tau>50Pa}$ and $I_{\tau>9Pa}$: fraction of fluid volume with scalar shear stresses above 150, 50 and 9 Pa, respectively, WSS: wall shear stress, $I_{WSS>1Pa}$: relative area of the impeller surface exposed to WSS above 1 Pa, HI: hemolysis index, $SPWVI$: spanwise vorticity index.
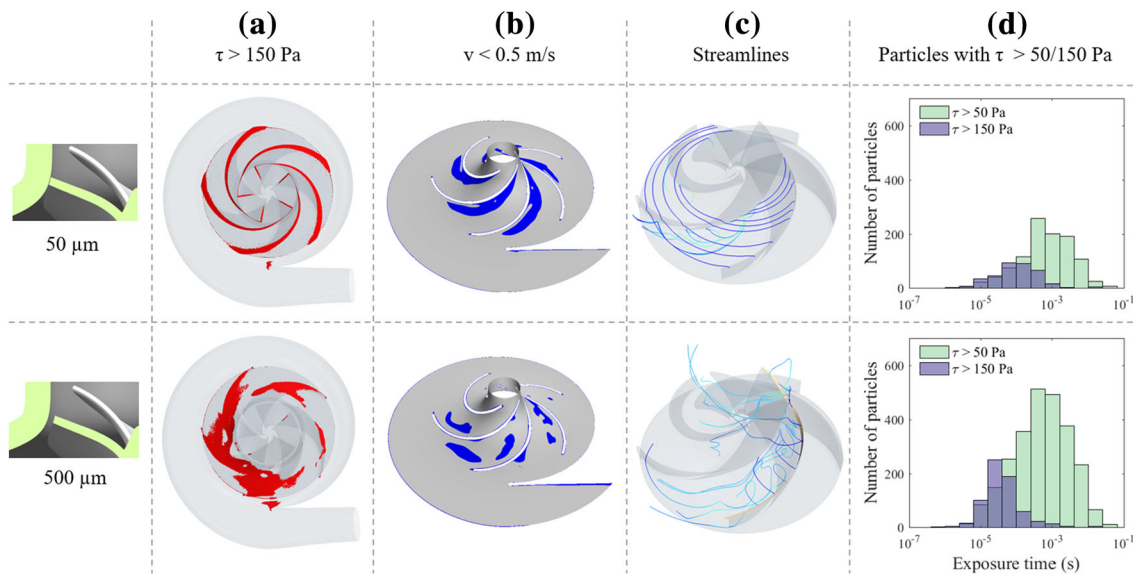
* $p < 0.05$, ** $p < 0.01$.

FIGURE 5. Visualization of the effects of change in clearance gap size from 50 to 500 μm. (a) Localization and extent of areas of high shear stress ($\tau > 150$ Pa). (b) Regions with low velocities ($v < 0.5$ m/s) along the meridional section of the flow channels inside the pump. The velocity threshold of 0.5 m/s was chosen for best visual representation of possible stagnation zones. (c) Flow structures represented by streamlines seeded with a randomized distribution in the clearance gap above one of the blades. (d) Histograms of the exposure times to shear stresses above 50 and 150 Pa. With the 50 μm clearance gap, 1049 (16.8%) and 364 (5.8%) of the seeded particles experienced SS above 50 and 150 Pa, respectively, compared to 2560 (40.2%) and 669 (10.5%) with the 500 μm gap.

stantial effects, followed by the change in shroud design.

Relative changes in hemocompatibility indicators are shown in Fig. 4. In this figure, all indices are normalized by their respective value in the baseline geometry to allow for a direct comparison of the relative impact of the various design variations. The numerical data, without normalization to the baseline geometry, is listed in Supplementary Material C. Fractions of fluid volume with shear stress values above a threshold, $I_{\tau>150Pa}$, $I_{\tau>50Pa}$ and $I_{\tau>9Pa}$, were
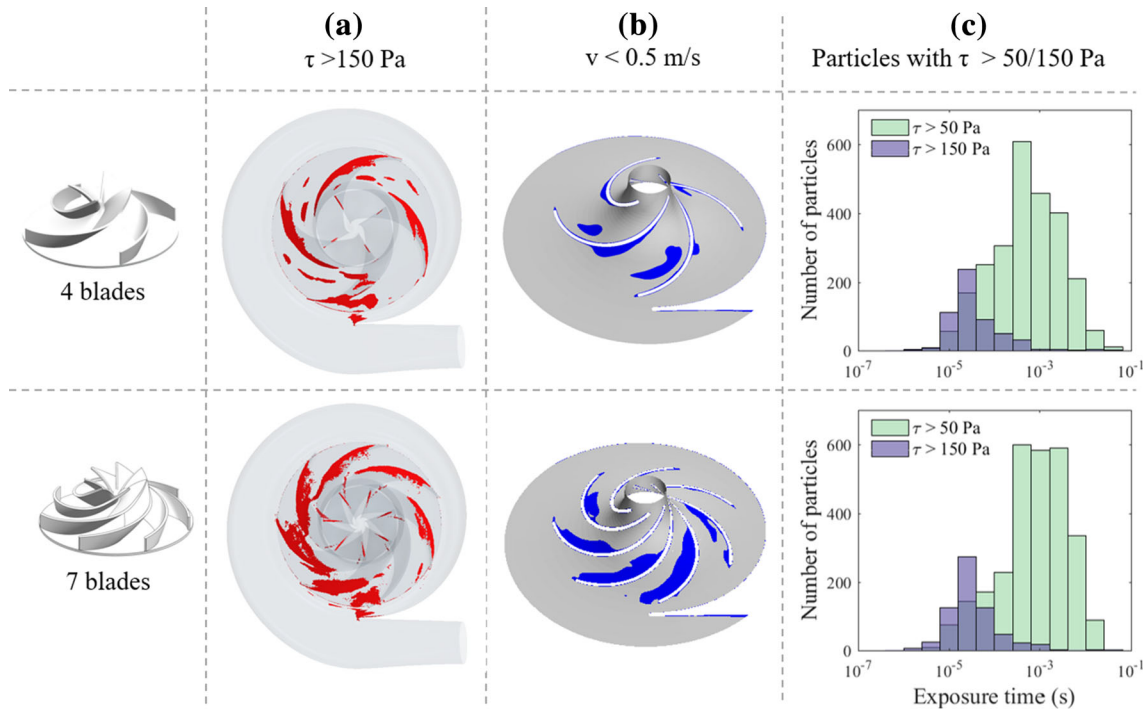
FIGURE 6. Visualization of the effects of change in the number of blades from 4 to 7. (a) Areas of high shear stress (τ > 150 Pa). (b) Regions with low velocities (< 0.5 m/s) along the meridional section of the flow channels inside the pump. The velocity threshold of 0.5 m/s was chosen for best visual representation of possible stagnation zones. (c) Histograms of the exposure times to shear stresses above 50 Pa and 150 Pa. With 4 blades, 2552 (40.3%) and 557 (8.8%) of the seeded particles experienced SS above 50 and 150 Pa, respectively, compared to 2835 (44.8%) and 651 (10.3%) with 7 blades.

in the range of 0.006–0.049%, 1.1–2.2%, and 14.4–16.6% of the total fluid volume, respectively.

Table 4 shows Spearman's rank correlation coefficients (r) between all derived metrics of pump performance and hemocompatibility. Strong positive correlations were found between HI and $I_{\tau > 50\text{Pa}}$ ($r = 0.74$, $p = 0.037$), and between SPWVI and $I_{\tau > 9\text{Pa}}$ ($r = 0.86$, $p = 0.007$). A strong negative relation was observed between HI and efficiency ($r = -0.71$, $p = 0.047$). None of the other correlations were found to be significant.

Clearance Gap Size

From the smallest clearance gap of 50 μm to the largest one of 500 μm, the flow rate decreased by 43% and the efficiency decreased by 28% (Fig. 3). Although the flow rate steadily declined from 5.7 L/min to 3.2 L/min, the efficiency remained constant at 53% for the two smaller gaps (50 and 150 μm), and only declined for larger ones, reducing to 38% for a gap of 500 μm.

Figure 5a depicts the fluid volume exposed to high shear stresses (SS), which in Fig. 4 was shown to be minimal for medium gap sizes (150, 300 μm). Yet, HI steadily increased with increasing gap size. In contrast, smaller gaps led to larger regions of low speeds (< 0.5 m/s, Fig. 5b). SPWVI was lowest for medium-sized gaps (Fig. 4). Larger clearance gaps induced significant flow disturbances on the suction side of the blade as shown by streamlines seeded just above a blade, whereas for the small clearance gap (50 μm) streamlines seeded at the same position were almost undisturbed (Fig. 5c). The number of particles exposed to medium (> 50 Pa) and high (> 150 Pa) SS increased substantially for the large gap (Fig. 5d). In contrast, large gaps reduced the maximum SS that particles were exposed to (Supplementary Material D).

Number of Blades

Increasing the blade number from four to seven increased the pump flow rate from 4.0 to 4.6 L/min (+ 15%), but did not affect efficiency (variation within ± 1%, Fig. 3). The values of $I_{\tau > 50\text{Pa}}$ and $I_{\tau > 9\text{Pa}}$ increased marginally with an increasing number of blades (Fig. 4). In contrast to $I_{\tau > 50\text{Pa}}$, the thrombosis indicators $I_{\text{WSS} < 1\text{Pa}}$ and SPWVI increased to 3.5-fold and 1.9-fold when the blade count was increased from 4 to 7. Stagnation zones with low velocity (Fig. 6b) increased with the number of blades and aggregated for higher blade numbers at the suction side of the blades. Exposure times to medium and high SS were almost unaffected, with a slight shift towards longer exposure to medium stresses for seven blades (Fig. 6c).
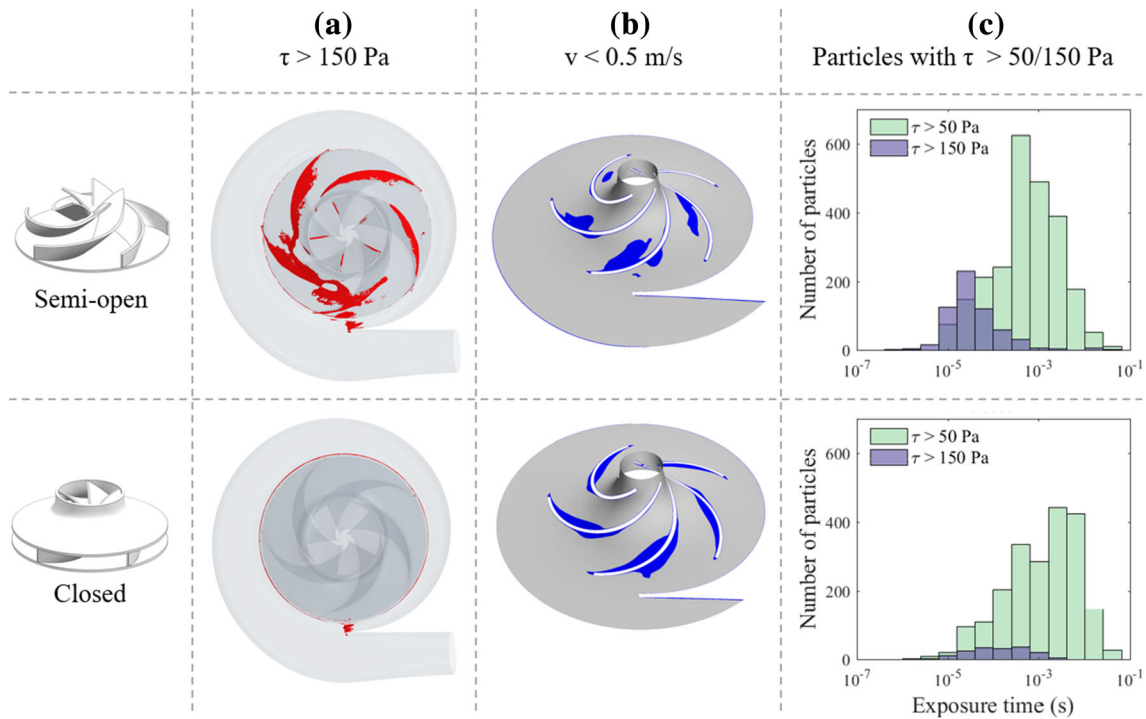
FIGURE 7. Visualization of the effect of a semi-open vs. closed shroud design. (a) Areas of high shear stress ($\tau > 150$ Pa). (b) Regions with low velocities ($v < 0.5$ m/s) along the meridional section of the flow channels inside the pump. The speed threshold of 0.5 m/s was chosen for best visual representation of possible stagnation zones. (c) Histograms of the exposure times to shear stresses above 50 and 150 Pa. With the semi-open design, 2435 (38.5%) and 611 (9.7%) of the seeded particles experienced SS above 50 and 150 Pa, respectively, compared to 2111 (33.0%) and 171 (2.7%) with the closed design.
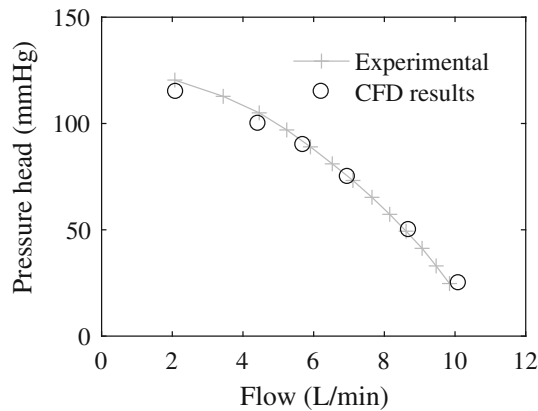

FIGURE 8. Experimental measurements and simulation results of the hydraulic performance of the baseline design at a rotational speed of 3000 rpm.

Shroud design

Compared to the semi-open impeller, the closed impeller yielded higher hydraulic efficiency and flow rate (Fig. 3). In the semi-open design, high SS occurred in the clearance gap, a behavior that was effectively suppressed by the closed design (Fig. 7a). The closed design also reduced the size of the low-velocity zones near the blades (Fig. 7b), but gave rise to stagnation zones at the corner edges where blades and shroud meet. The closed impeller radically reduced the amount of fluid exposed to SS above 150 Pa, but moderately increased the amount of fluid exposed to mid-range SS above 50 Pa, and more than tripled the value of low WSS $I_{WSS<1}$ (Fig. 4). Similarly, substantially fewer particles were exposed to high SS for the closed design, while simultaneously, exposure time to medium SS increased (Fig. 7c).

Validation

We compared simulated and measured pump performance with the baseline geometry, finding good agreement between the two modalities. For a speed of 3000 rpm and a pressure head of 100 mmHg, the simulated flow rate was 4.4 vs. 4.9 L/min in the experiments, which corresponds to a difference of 10.3%. Figure 8 shows the experimental measurements of the relation between pressure head and flow rate at a rotational speed of 3000 rpm. A curve shape that is typical for radial pumps can be observed, flatter at low and steeper at high flow rates. The difference between experimentally measured and simulated flow rates is high in the low flow region (< 5 L/min) with 19.7% root mean square error compared to only 2.4% in the high flow region (> 5 L/min).

DISCUSSION

In this study, we performed systematic variations of design parameters in a centrifugal blood pump. Using CFD, we analysed their effects on the flow field and multiple metrics of hydraulic performance. Exposure to elevated shear stress and exposure duration have been shown to damage and/or activate the cellular components of blood including erythrocytes, thrombocytes[9] and leukocytes.[7] According to Virchow's triad of thrombus formation, zones of low flow require attention. Despite the evidence for flow induced blood damage, validated models for predictions of measured values of damage remain a challenge. While indices such as the numerically derived hemolysis index often provide an integrated view on specific flow features, they should not be interpreted as predictors of measured blood damage. We, therefore, use them here in combination with detailed analysis of the flow fields and particle tracks to shed light on the influence of each independent design variation on the extent of cell exposure to potentially damaging or activating hemodynamic environments.

In the choice of clearance gap size, designers face conflicting requirements: Aiming for high hydraulic efficiency calls for small gaps, whereas minimization of maximum SS and suspected washout performance would suggest larger gaps. In our geometries, smaller gap sizes indeed increased the maximum SS (Supplementary Material D). However, firstly, the total fluid volumes exposed to high SS ($I_{\tau > 150\text{Pa}}$) were comparable for 50 and 500 μm gaps (Fig. 4) and, secondly, smaller gaps induced cell screening, an effect also observed experimentally by Antaki *et al.*,[1] such that only half as many particles effectively experienced these high SS in the 50 μm gap compared to the 500 μm gap (5.8% vs. 10.5% of the tracks, Fig. 5d). Larger gaps on the other hand gave rise to substantial flow disturbances in the fluid path (Fig. 5c), increasing SS and vorticity. As a result, volumes exposed to medium SS ($I_{\tau > 50\text{Pa}}$) generally increased with gap size. These medium SS volumes, with sizes two to three orders of magnitude larger than those with SS above 150 Pa, affected about 40% of the particles in the 500 μm gap setup vs. only 17% in the 50 μm gap configuration (Fig. 5d). Increased vorticity content in the main particle paths is reflected by the increase in SPWVI with the largest gap size. Combined, the noted changes in SS histories led to lower HI in smaller gaps, which is consistent with previous results.[11] In contrast, Wu *et al.*[31] reported minimal HI at 100 μm compared to clearance gaps of 50 and 200 μm. Different to our study, they studied the effect of gap size

prescribing a constant flow rate. While a well validated metric of hemolysis remains to be established, all qualitative and quantitative indicators investigated here suggest that by minimizing the number of cells exposed to high and medium stresses, smaller gaps may be expected to yield lower hemolysis than larger ones. This is also consistent with experimental observations.[16] SS > 50 Pa and higher SPWVI have been proposed as indicators of platelet activation. However, whether the noted reduction in $I_{\tau > 50\text{Pa}}$ and SPWVI (Fig. 4) in the 50 μm gap compared to the 500 μm gap geometry do translate into reduced activation remains to be demonstrated. One major drawback of the smaller gaps is certainly the close to three-fold increase in regions of low WSS and flow separation with low velocities on the pressure side of the blades. Strategies to avoid stagnation regions should thus be devised in accordance to the retained gap size. The gap size also affected the location of potential flow stagnation regions, shifting from the pressure side in the 50 μm to centrally in the vanes in the 500 μm gap (Fig. 5b).

Compared to gap size variations, varying the number of blades had more blunted effects. While there was a clear increase in volumes exposed to high SS with 7 blades compared to 4, SS histograms were almost unaffected, showing for 7 blades only a slight shift towards longer exposure times to medium stresses (Fig. 6c). Consistent with these marginal changes in SS exposures, HI was also marginally affected. The SPWVI increased with the number of blades, as did the regions of potential flow stagnations ($I_{\text{WSS} < 1\text{Pa}}$, Fig. 4) due to flow separation at each blade (Fig. 6b). Collectively, the decreased SS, vorticity indices and extent of potential stagnation zones point to fewer blades as being advantageous in terms of potential hemocompatibility. However, it should be noted that for fewer than 5 blades this comes at the cost of a decrease in pump flow rate.

In contrast to the above, shroud design variations yielded conflicting observations. Compared to the semi-open design, a closed shroud drastically reduced exposure to high SS but increased exposure time to medium SS (Fig. 7c). The number of particles affected by medium SS was one order of magnitude larger than to the peak SS. HI was slightly lower for the semi-open configuration reflecting the opposite evolution of exposures to high and medium SS. However, without further data, no conclusion can be drawn on the integrated effect of these two changes on net hemolysis. Both platelet activation indicators suggested slightly preferable behaviour for the semi-open shroud. The

semi-open compared to the closed design resulted in a smaller overall area of low WSS.

Overall, statistical analysis revealed that high efficiency correlates with low HI ($r = -0.71$, $p = 0.047$). Indeed, more efficient pumps have fewer recirculation zones, flow disturbances and lower leakage flow, all of which contribute to higher shear stresses or longer exposure times and thereby higher HI. This finding is consistent with the experimental data of Mozafari et al.[22] Lack of correlation between HI and $I_{\tau > 150\text{Pa}}$ ($r = -0.12$, $p = 0.78$) highlights that in the considered geometries, peak SS only reflects a small part of particles' SS histories, which are dominated by medium stresses as indicated by the correlation of HI and $I_{\tau > 50\text{Pa}}$ ($r = .74$, $p = .037$) and the areas under the histograms in Fig. 5d. The two metrics that have been suggested to indicate platelet activation, $I_{\tau > 50\text{Pa}}$ and SPWVI, did not correlate ($r = 0.21$, $p = 0.61$) in our study.

The computational approach employed in this study has limitations. First and foremost, all design variations were tested against a constant pressure head. The consideration of pulsatile conditions would be an important next step, acknowledging not only the physiological pulsations in the cardiovascular system, but also VAD-inherent features such as washout algorithms as in the HM3.[19] Secondly, while the blood damage indicators used in this study are widely employed in cardiovascular modelling, they remain explorative. They substantially simplify complex biological mechanisms [8,27] and often perform poorly when evaluated against experimental data.[27] We, therefore, used them here to probe integrated flow characteristics rather then as predictors of measured blood damage. Quantification of true hemolysis or platelet activation potentials requires further investigation. Further effects, such as the interaction between blood and the pump material are also critical for thrombogenesis [13] and hemocompatibility. Biological advances in its understanding and modelling could significantly enhance the predictive power of CFD models. Finally, we investigated an approach presented recently, which links SPWVI to platelet activation.[21] We applied this metric to Lagrangian tracks of particles with properties similar to erythrocytes (diameter 5 μm, density 1125 kg/m^3) rather than platelets (1 μm, simulated as massless) as used in the original work. Even though this might slightly alter the flow paths, the major characteristics of the tracks are expected to remain unaffected. However, the SPWVI lacks a thorough experimental validation. Thus, the prediction of platelet activation remains challenging and requires further investigation.

ELECTRONIC SUPPLEMENTARY MATERIAL

The online version of this article (https://doi.org/10.1007/s10439-017-1951-0) contains supplementary material, which is available to authorized users.

REFERENCES

[1]Antaki, J. F., C. G. Diao, F. J. Shu, J. C. Wu, R. Zhao, and M. V. Kameneva. Microhaemodynamics within the blade tip clearance of a centrifugal turbodynamic blood pump. *Proc. Inst. Mech. Eng. Part H J. Eng. Med.* 222:573–581, 2008.

[2]Arvand, A., N. Hahn, M. Hormes, M. Akdis, M. Martin, and H. Reul. Comparison of hydraulic and hemolytic properties of different impeller designs of an implantable rotary blood pump by computational fluid dynamics. *Artif. Organs* 28:892–898, 2004.

[3]Bludszuweit, C. Three dimensional numerical prediction of stress loading of blood particles in a centrifugal pump. *Artif. Organs* 19:590–596, 1995.

[4]Bluestein, D., K. B. Chandran, and K. B. Manning. Towards non-thrombogenic performance of blood recirculating devices. *Ann. Biomed. Eng.* 38:1236–1256, 2010.

[5]Boës, S., G. Ochsner, R. Amacher, A. Petrou, M. Meboldt, and M. Schmid Daners. Control of the fluid viscosity in a mock circulation. *Artif. Organs* 1:10, 2017.

[6]Chan, W. K., Y. W. Wong, Y. Ding, L. P. Chua, and S. C. M. Yu. Numerical investigation of the effect of blade geometry on blood trauma in a centrifugal blood pump. *Artif. Organs* 26:785–793, 2002.

[7]Dewitz, T. S., T. C. Hung, R. R. Martin, and L. V. McIntire. Mechanical trauma in leukocytes. *J. Lab. Clin. Med.* 90:728–736, 1977.

[8]Fraser, K. H., M. E. Taskin, B. P. Griffith, and Z. J. Wu. The use of computational fluid dynamics in the development of ventricular assist devices. *Med. Eng. Phys.* 33:263–280, 2011.

[9]Fraser, K. H., T. Zhang, M. E. Taskin, B. P. Griffith, and Z. J. Wu. A Quantitative comparison of mechanical blood damage parameters in rotary ventricular assist devices: shear stress, exposure time and hemolysis index. *J. Biomech. Eng.* 134:081002, 2012.

[10]Garon, A., and M.-I. Farinas. Fast three-dimensional numerical hemolysis approximation. *Artif. Organs* 28:1016–1025, 2004.

[11]Graefe, R., A. Henseler, and U. Steinseifer. Multivariate assessment of the effect of pump design and pump gap design parameters on blood trauma. *Artif. Organs* 40:568–576, 2016.

[12]Gülich, J. F. Centrifugal Pumps. Berlin Heidelberg: Springer, 2010. doi:10.1017/CBO9781107415324.004.

[13]Hellums, J. D. 1993 Whitaker lecture: biorheology in thrombosis research. *Ann. Biomed. Eng.* 22:445–455, 1994.

[14]Heuser, G., and R. Opitz. A Couette viscometer for short time shearing of blood. *Biorheology* 17:17–24, 1980.

[15]Hochareon, P., K. B. Manning, A. A. Fontaine, J. M. Tarbell, and S. Deutsch. Correlation of in vivo clot deposition with the flow characteristics in the 50 cc Penn State artificial heart: a preliminary study. *ASAIO J.* 50:537–542, 2004.

[16]Kim, N. J., C. Diao, K. H. Ahn, S. J. Lee, M. V. Kameneva, and J. F. Antaki. Parametric study of blade tip clearance, flow rate, and impeller speed on blood damage in rotary blood pump. *Artif. Organs* 33:468–474, 2009.

[17]Kirklin, J. K., D. C. Naftel, F. D. Pagani, R. L. Kormos, L. W. Stevenson, E. D. Blume, S. L. Myers, M. A. Miller, J. T. Baldwin, and J. B. Young. Seventh INTERMACS annual report: 15,000 patients and counting. *J. Hear. Lung Transplant.* 34:1495–1504, 2015.

[18]Korakianitis, T., M. A. Rezaienia, G. M. Paul, A. Rahideh, M. T. Rothman, and S. Mozafari. Optimization of centrifugal pump characteristic dimensions for mechanical circulatory support devices. *ASAIO J.* 62:545–551, 2016.

[19]Krabatsch, T., J. D. Schmitto, Y. Pya, D. Zimpfer, J. Garbade, V. Rao, M. Morshuis, S. Marasco, F. Beyersdorf, P. Sood, L. Damme, and I. Netuka. Heartmate 3 fully magnetically levitated left ventricular assist device for the treatment of advanced heart failure-1 year results from the CE mark trial. *J. Hear. Lung Transplant.* 35:S9, 2016.

[20]Merrill, E. W. Rheology of blood. *Physiol. Rev.* 49:836–886, 1969.

[21]Morbiducci, U., R. Ponzini, M. Nobili, D. Massai, F. M. Montevecchi, D. Bluestein, and A. Redaelli. Blood damage safety of prosthetic heart valves. Shear-induced platelet activation and local flow dynamics: a fluid-structure interaction approach. *J. Biomech.* 42:1952–1960, 2009.

[22]Mozafari, S., M. A. Rezaienia, G. M. Paul, M. T. Rothman, P. Wen, and T. Korakianitis. The effect of geometry on the efficiency and hemolysis of centrifugal implantable blood pumps. *ASAIO J.* 63:53–59, 2017.

[23]Nascimbene, A., S. Neelamegham, O. H. Frazier, J. L. Moake, and J. Dong. Acquired von Willebrand syndrome associated with left ventricular assist device. *Blood* 127:3133–3142, 2016.

[24]Nobili, M., U. Morbiducci, R. Ponzini, C. Del Gaudio, A. Balducci, M. Grigioni, F. Maria Montevecchi, and A. Redaelli. Numerical simulation of the dynamics of a bileaflet prosthetic heart valve using a fluid-structure interaction approach. *J. Biomech.* 41:2539–2550, 2008.

[25]Ochsner, G., R. Amacher, A. Amstutz, A. Plass, M. Schmid Daners, H. Tevaearai, S. Vandenberghe, M. J. Wilhelm, and L. Guzzella. A novel interface for hybrid mock circulations to evaluate ventricular assist devices. *IEEE Trans. Biomed. Eng.* 60:507–516, 2013.

[26]Schmitto, J. D., J. S. Hanke, S. V. Rojas, M. Avsar, and A. Haverich. First implantation in man of a new magnetically levitated left ventricular assist device (HeartMate III). *J. Hear. Lung Transplant.* 34:858–860, 2015.

[27]Taskin, M. E., K. H. Fraser, T. Zhang, C. Wu, B. P. Griffith, and Z. J. Wu. Evaluation of Eulerian and Lagrangian models for hemolysis estimation. *ASAIO J.* 58:363–372, 2012.

[28]Thamsen, B., B. Blümel, J. Schaller, C. O. Paschereit, K. Affeld, L. Goubergrits, and U. Kertzscher. Numerical analysis of blood damage potential of the HeartMate II and HeartWare HVAD Rotary blood pumps. *Artif. Organs* 39:651–659, 2015.

[29]Wu, J., J. F. Antaki, J. Verkaik, S. Snyder, and M. Ricci. Computational fluid dynamics-based design optimization for an implantable miniature Maglev pediatric ventricular assist device. *J. Fluids Eng.* 134:041101, 2012.

[30]Wu, J., J. F. Antaki, W. R. Wagner, T. A. Snyder, B. W. Paden, and H. S. Borovetz. Elimination of adverse leakage flow in a miniature pediatric centrifugal blood pump by computational fluid dynamics-based design optimization. *ASAIO J.* 51:636–643, 2005.

[31]Wu, J., B. E. Paden, H. S. Borovetz, and J. F. Antaki. Computational fluid dynamics analysis of blade tip clearances on hemodynamic performance and blood damage in a centrifugal ventricular assist device. *Artif. Organs* 34:402–411, 2009.

[32]Wu, J., K. Shimmei, K. Tani, K. Niikura, and J. Sato. CFD-based design optimization for hydro turbines. *J. Fluids Eng.* 129:159–168, 2007.

[33]Yu, H., G. Janiga, and D. Thévenin. Computational fluid dynamics-based design optimization method for archimedes screw blood pumps. *Artif. Organs* 40:341–352, 2016.